Video Article

Quantitative Magnetic Resonance Imaging of Skeletal Muscle Disease

Bruce M. Damon[1,2,3,4], Ke Li[1,2], Richard D. Dortch[1,2], E. Brian Welch[1,2], Jane H. Park[1,2,4], Amanda K. W. Buck[1,2], Theodore F. Towse[1,2,5], Mark D. Does[1,2,3], Daniel F. Gochberg[1,2,6], Nathan D. Bryant[1,2]

[1]Institute of Imaging Science, Vanderbilt University

[2]Department of Radiology and Radiological Sciences, Vanderbilt University

[3]Department of Biomedical Engineering, Vanderbilt University

[4]Department of Molecular Physiology and Biophysics, Vanderbilt University

[5]Department of Physical Medicine and Rehabilitation, Vanderbilt University

[6]Department of Physics and Astronomy, Vanderbilt University

Correspondence to: Bruce M. Damon at bruce.damon@vanderbilt.edu

URL: http://www.jove.com/video/52352
DOI: doi:10.3791/52352

Keywords: Medicine, Issue 118, DT-MRI, MT, FWMRI, atrophy, fat replacement, biophysical basis, neuromuscular disorders, inflammatory myopathies, muscular dystrophy

Date Published: 12/18/2016

Citation: Damon, B.M., Li, K., Dortch, R.D., Welch, E.B., Park, J.H., Buck, A.K., Towse, T.F., Does, M.D., Gochberg, D.F., Bryant, N.D. Quantitative Magnetic Resonance Imaging of Skeletal Muscle Disease. *J. Vis. Exp.* (118), e52352, doi:10.3791/52352 (2016).

Abstract

Quantitative magnetic resonance imaging (qMRI) describes the development and use of MRI to quantify physical, chemical, and/or biological properties of living systems. Neuromuscular diseases often exhibit a temporally varying, spatially heterogeneous, and multi-faceted pathology. The goal of this protocol is to characterize this pathology using qMRI methods. The MRI acquisition protocol begins with localizer images (used to locate the position of the body and tissue of interest within the MRI system), quality control measurements of relevant magnetic field distributions, and structural imaging for general anatomical characterization. The qMRI portion of the protocol includes measurements of the longitudinal and transverse relaxation time constants (T1 and T2, respectively). Also acquired are diffusion-tensor MRI data, in which water diffusivity is measured and used to infer pathological processes such as edema. Quantitative magnetization transfer imaging is used to characterize the relative tissue content of macromolecular and free water protons. Lastly, fat-water MRI methods are used to characterize fibro-adipose tissue replacement of muscle. In addition to describing the data acquisition and analysis procedures, this paper also discusses the potential problems associated with these methods, the analysis and interpretation of the data, MRI safety, and strategies for artifact reduction and protocol optimization.

Video Link

The video component of this article can be found at http://www.jove.com/video/52352/

Introduction

Quantitative magnetic resonance imaging (qMRI) describes the development and use of MRI to quantify physical, chemical, and/or biological properties of living systems. QMRI requires that one adopt a biophysical model for the system, composed of the tissue of interest and an MRI pulse sequence. The pulse sequence is designed to sensitize the images' signal intensities to the parameter of interest in the model. MRI signal properties (signal magnitude, frequency, and/or phase) are measured and analyzed according to the model. The goal is to produce an unbiased, quantitative estimate of a physical or biological parameter having continuously distributed, physical units of measurement. Often the equations describing the system are analyzed and fitted on a pixel-by-pixel basis, producing an image whose pixel values directly reflect the values of the variable. Such an image is referred to as a parametric map.

A common use of qMRI is the development and application of biomarkers. Biomarkers can be used to investigate a disease mechanism, establish a diagnosis, determine a prognosis, and/or assess a therapeutic response. They may take the form of the concentrations or activities of endogenous or exogenous molecules, a histological specimen, a physical quantity, or an internal image. Some general requirements of biomarkers are that they objectively measure a continuously distributed variable using physical units of measurement; have a clear, well understood relationship with the pathology of interest; are sensitive to improvement to and worsening of clinical state; and can be measured with suitable accuracy and precision. Non-invasive or minimally invasive biomarkers are particularly desirable, as they promote patient comfort and minimally disturb the pathology of interest.

A goal for developing image-based biomarkers for muscle disease is to reflect muscle disease in ways that are complementary to, more specific than, more spatially selective than, and/or less invasive than existing approaches. One particular advantage of qMRI in this regard is that it has the potential to integrate multiple types of information and thus potentially characterize many aspects of the disease process. This ability is very important in muscle diseases, which frequently exhibit a spatially variable, complex pathology that includes inflammation, necrosis and/or atrophy with fat replacement, fibrosis, disruption of the myofilament lattice ("Z-disk streaming"), and membrane damage. Another advantage of

Copyright © 2016 Journal of Visualized Experiments

qMRI methods is that qualitative or semi-quantitative descriptions of contrast-based MR images reflect not just pathology, but also differences in image acquisition parameters, hardware, and human perception. An example of this last issue was demonstrated by Wokke *et al*., who showed that semi-quantitative assessments of fat infiltration are highly variable and frequently incorrect, when compared with quantitative fat/water MRI (FWMRI)[1].

The protocol described here includes pulse sequences for measuring the longitudinal (T_1) and transverse (T_2) relaxation time constants, quantitative magnetization transfer (qMT) parameters, water diffusion coefficients using diffusion tensor MRI (DT-MRI), and muscle structure using structural images and FWMRI. T_1 is measured by using an inversion recovery sequence, in which the net magnetization vector is inverted and its magnitude is sampled as the system returns to equilibrium. T_2 is measured by repeatedly refocusing transverse magnetization using a train of refocusing pulses, such as the Carr-Purcell Meiboom-Gill (CPMG) method, and sampling the resulting spin-echoes. T_1 and T_2 data can be analyzed using non-linear curve-fitting methods that either assume a number of exponential components *a priori* (typically between one and three) or by using a linear inverse approach which fits the observed data to the sum of a large number of decaying exponentials, resulting in a spectrum of signal amplitudes. This approach requires a non-negative least square (NNLS) solution[3], and typically includes additional regularization to produce stable results. T_1 and T_2 measurements have been widely used to study muscle diseases and injury[4-9]. T_1 values are typically decreased in fat-infiltrated regions of muscle and elevated in inflamed regions[4-6]; T_2 values are elevated in both fat-infiltrated and inflamed regions[10].

QMT-MRI characterizes the free water and solid-like macromolecular proton pools in tissues by estimating the ratio of macromolecular to free water protons (the pool size ratio, PSR); the intrinsic relaxation rates of these pools; and the rates of exchange between them. Common qMT approaches include pulsed saturation[11] and selective inversion recovery[12,13] methods. The protocol below describes use of the pulsed saturation approach, which exploits the broad linewidth of the macromolecular proton signal, relative to the narrow linewidth of the water proton signal. By saturating the macromolecular signal at resonance frequencies sufficiently different from the water signal, the water signal is reduced as a result of magnetization transfer between the solid and free water proton pools. The data are analyzed using a quantitative biophysical model. QMT has been developed and applied in healthy muscles[14,15], and a recent abstract appeared describing its implementation in muscle disease[16]. QMT has been used to study small animal models of muscle inflammation, wherein it has been shown that inflammation decreases the PSR[17]. Inasmuch as MT reflects both macromolecular and water contents, MT data may also reflect fibrosis[18,19].

DT-MRI is used to quantify the anisotropic diffusion behavior of water molecules in tissues with ordered, elongated cells. In DT-MRI, water diffusion is measured in six or more different directions; these signals are then fitted to a tensor model[20]. The diffusion tensor, **D**, is diagonalized to obtain three eigenvalues (which are the three principal diffusivities) and three eigenvectors (which indicate the directions corresponding to the three diffusion coefficients). These and other quantitative indices derived from **D** provide information about tissue structure and orientation at a microscopic level. The diffusion properties of muscle, especially the third eigenvalue of **D** and the degree of diffusion anisotropy, reflect muscle inflammation[17] and muscle damage due to experimental injury[21], strain injury[22], and disease[23,24]. Other potential influences on the diffusion properties of muscle include changes in cell diameter[25] and membrane permeability changes.

Lastly, muscle atrophy, without or without macroscopic fat infiltration, is a pathological component of many muscle diseases. Muscle atrophy can be evaluated by using structural images to measure muscle cross-sectional area or volume and FW-MRI to assess fatty infiltration. Fat infiltration can be qualitatively described in T_1- and T_2-weighted images[26], but fat and water signals are best measured by forming images that exploit the different resonance frequencies of fat and water protons[27-29]. Quantitative fat/water imaging methods have been applied in muscle diseases such as muscular dystrophy[1,30,31], and can predict the loss of ambulation in these patients[31].

The qMRI protocol described here uses all of these measurements to characterize muscle condition in the autoimmune inflammatory myopathies dermatomyositis (DM) and polymyositis (PM). Further details of the protocol, including its reproducibility, have been published previously[32]. The protocol includes standard pulse sequences as well as radiofrequency (RF) and magnetic field gradient objects specifically programmed on our systems. The authors anticipate that the protocol is also applicable in other neuromuscular disorders characterized by muscle atrophy, inflammation, and fat infiltration (such as the muscular dystrophies).

Protocol

NOTE: The reader is reminded that all research involving human subjects must be approved by the local Institutional Review Board (IRB) for the Use of Human Subjects in Research. Research participants must be informed of the purpose, procedures, risks, and benefits of the proposed research; the availability of alternative treatments or procedures; the availability of remuneration; and of their rights to privacy and to withdraw their consent and discontinue their participation. Prior to the MRI testing session, an investigator must present a potential research participant with an IRB-approved informed consent document (ICD), explain its contents, and ask the potential research participant if he/she wishes to participate in the study. If so, the participant will have to sign and date the ICD prior to completing any of the steps of the protocol here.

1. Actions Prior to the Day of Testing

1. **Restrict Lifestyle Habits that Could Confound the Data**
    1. Instruct the participant not to perform moderate or heavy exercise during the 48 h prior to testing. Instruct the participant to abstain from over-the-counter medication and alcohol intake during the 24 h prior to testing. Instruct the participant to refrain from tobacco use or caffeine consumption during the 6 h prior to testing.
    2. Prior to testing, confirm that the participant has been compliant with these instructions.

2. **Prepare the MRI System**
    1. Ensure the availability of all necessary equipment, as listed in the **Table of Materials and Equipment**.
    2. Define an MRI protocol; suggested parameters are found in **Tables 1 - 5**.

2. Day of Testing: Prepare for MRI Data Acquisition

1. **Conduct Safety Screening**
    1. Screen for potential hazards in the MRI environment by having an MRI safety-trained healthcare worker present the research participant with a suitable MRI safety form, such as that found at www.mrisafety.com.
    2. If there any implanted magnetic or magnetically sensitive objects, ensure that they are safe for MRI scanning.

2. **Prepare the MRI System**
    1. Ensure that all personnel have removed all magnetic and magnetically sensitive objects before entering the room that houses the MRI system. Conduct this check every time that someone enters the MRI room.
    2. Prepare the MRI system by placing the receive coil on the patient bed of the MRI system. Also, place a mattress with sheet and pillow with pillowcase on the bed. Have straps available to place around the thighs and bolsters or pillows to place under the knees.
    3. Start the software interface, enter patient data, and open the imaging protocol.

3. **Position the Research Participant on the MRI Scanner Table**
    1. Observe the research participant as he/she checks his/her person and clothing for magnetically sensitive objects. Secure these objects outside of the MRI room in a lockable container. Enter the MRI room with the research participant immediately after completing this step.
    2. Position the participant on the patient bed in a supine, feet-first position. Place the body part to be imaged as close to the midline of the table as practical. Place bolsters or pillows under the knees to provide strain relief for the lower back and place a pillow under the head. To limit motion, gently but effectively secure the thigh, leg, and feet and ensure that the participant is comfortable.
    3. Place the RF receiver coil around the participant's thighs and connect it to the MRI system.

4. **Instruct the Participant and Complete Final Pre-testing Steps**
    1. Give instructions about how to communicate with the investigators. Provide the participant with hearing protection and a signaling device that can be used to call for attention if needed. Instruct the participant of the need to stay still during and between all imaging sequences.
    2. Advance the patient bed into the MRI scanner such that the body part to be imaged is aligned to the center of the MRI scanner.
    3. After exiting the MRI room, confirm that the patient communication system is working and see that the participant is comfortable. Throughout the protocol, communicate regularly with the participant to ensure his/her comfort and compliance with instructions.

3. Day of Testing: Acquire the MRI Data

1. **Preparatory Steps**
    1. As the MRI system determines the instrumental settings and calibrations prior to each imaging sequence (center frequency, receiver gain calibration, *etc.*), supervise these processes and ensure that each step is being performed correctly.
    2. Using a suitable software interface, acquire a set of localizer images (also known as pilot or scout images); using suggested parameters presented in **Table 2**.
    3. Determine where to place the center slice for qMRI data acquisitions, by identifying areas of damage and/or by referencing the slice position relative to reproducible anatomical landmarks.

2. **Transmit and Receive Coil Calibration Steps**
    1. For these steps as well as all of the subsequent imaging steps, define region of anatomy in which to optimize the homogeneity of the static magnetic field (B_0), a process known as "shimming". See **Figure 1A** for the typical placement of the shimming volume of interest (VOI) used in the present studies.
    2. If the MRI scanner has a multi-element transmission coil, acquire an RF calibration dataset.
    3. If the MRI scanner has a multi-element receive coil, acquire a spatial sensitivity map of the coils.

3. **Acquire Structural MRI Data**
    1. Acquire high resolution, multi-slice, T_1-weighted images using a fast spin-echo (FSE) sequence; the imaging parameters used in the present studies are provided in **Table 1.**
    2. Acquire high resolution, multi-slice, T_2-weighted images using an FSE sequence; the imaging parameters used in the present studies are provided in **Table 2**.

4. **Acquire Data for Real-time Quality Control and Making Post-processing Corrections**
    1. Acquire three-dimensional (3D) multiple gradient-echo data for the calculation of B_0 field maps. The imaging parameters used in the present studies are provided in **Table 3**.
    2. Examine the field maps to ensure that there are no deviations of greater than ±60 Hz (approximately 0.5 parts per million at 3 Tesla) across the image. If there are, adopt an alternative approach to shimming (different method, different placement of VOI, *etc.*).
    3. Acquire 3D data for the calculation of nutation angle maps. The imaging parameters used in the present studies are provided in **Table 2**.
    4. Examine the field maps to ensure that there are no areas that deviate excessively from the nominal nutation angle. For the RF pulses that are used in this protocol, deviations greater than ± 30% of the nominal nutation angle are considered excessive.

5. **Acquire the qMRI Data**
    1. Acquire 3D images for calculation of the T_1, using an inversion recovery sequence. The imaging parameters used in the present studies are presented in **Table 3**.
    2. Repeat the T_1 measurement in the presence of fat signal suppression (FS; this parameter is abbreviated $T_{1,FS}$).

3. Acquire single-slice images for calculation of the T_2, using a multiple spin-echo sequence. Use the imaging parameters presented in **Table 3**.
4. Repeat the T_2 measurement in the presence of FS ($T_{2,FS}$).
5. Acquire 3D images for calculation of qMT parameters, using a pulsed saturation sequence with FS and the imaging parameters given in **Table 4**.
6. Acquire multi-slice data for calculation of diffusion-tensor parameters, using a series of diffusion-weighted images. The imaging parameters used in these studies are given in **Table 4**.
7. Acquire 3D data for calculation of fat/water images, using a series of six gradient-echo images. The imaging parameters used in these studies are given in **Table 5**.

6. **After Completing the qMRI Protocol**
   1. Ensure that all images are of suitable quality by examining them for potentially correctable artifacts and by measuring the sufficient signal-to-noise ratio.
   2. For each qMRI dataset, define several regions of interest (ROIs) in the image series and examine the signal as a function of the relevant parameter (for example, for the T_1-dependent data acquired in steps 3.5.1 and 3.5.2, plot the signal as a function of TI and ensure that the data follow the inversion-recovery function listed below in step 4.1.2).
   3. After completing a personal screening for magnetically sensitive objects, enter the MRI room. Remove the participant from the magnet, remove all straps and padding, and assist the participant in exiting the MRI scanner and the MRI room.
   4. Transfer the data, using methods compliant with local health privacy laws, to a local workstation for processing; data may be exported as Digital Imaging Communications in Medicine (DICOM) files or in the vendor's proprietary format (the method used in this protocol).

4. Analyze the qMRI Data

1. **Calculate the Parametric Maps**
   1. Use a computer program designed for scientific computing and image analysis. By examining a histogram of the signal intensities in the image, form a signal threshold-based image mask that delineates areas of signal from areas of noise. Complete the steps below for every pixel in the signal portions of the images.
   2. Analyze the T_1 data by measuring the signal intensity S for each inversion time (TI). Then, fit the values for S to an inversion-recovery with reduced pre-delay model:
   $$S = M_0\left[S_f\left(1 - e^{-TD/T_1}\right)e^{-TI/T_1} + 1 - e^{-TI/T_1}\right] \quad [1]$$
   where M_0 is a signal intensity representing the magnetization at the equilibrium state, S_f is the inversion ratio, and TD is the pre-delay time. Then, fit the data with FS to the same model, allowing determination of the longitudinal relaxation time constant with FS, $T_{1,FS}$.
   3. Analyze the T_2 data by measuring S at each TE. Then, fit the data to a mono-exponential decay model:
   $$S = M_0 e^{-TE/T_2} + N \quad [2a]$$
   where N is the signal offset at baseline. The reader may also decide to fit the data to a multi-exponential model, such as that below:
   $$S = \mathrm{N} + M_0 \sum_{j=1}^{J} f_j e^{-TE/T_{2,j}} \quad [2b]$$
   where J is the number of exponential components and f and $T_{2,j}$ are the signal fraction and T_2 values associated with the jth component. Or, the reader may use a non-negative least squares (NNLS) method[3]. In the latter case, the Multi-exponential Relaxation Analysis (MERA) toolbox[33] is freely available; other programs are available too. Repeat these analyses for the data with and without FS.
   4. To analyze the qMT data, measure S for each irradiation power and frequency offset. Correct the nominal irradiation powers (represented by ω_1 in the equation below) using the nutation angle maps. Correct the frequency offsets (Δf in the equation below) by using the B_0 maps to adjust the applied offset frequencies. Then, fit the data to the following model[34,35]
   $$S(\omega_1, \Delta f) = \frac{S_0\left(R_B\left[\frac{RM_0^A F}{R_A}\right] + R_{RFB} + R_B + RM_0^A\right)}{\left[\frac{RM_0^A F}{R_A}\right](R_B + R_{RFB}) + \left(1 + \left[\frac{\omega_{1CWPE}}{2\pi\Delta f}\right]^2\left[\frac{1}{R_2 T_2^A}\right]\right)(R_{RFB} + R_B + RM_0^A)} \quad [3]$$
   where is the exchange rate from the macromolecular pool to the free water pool, is the longitudinal relaxation rate of the free water pool, is the longitudinal relaxation rate of the macromolecular pool (assumed to be 1 s^{-1}), is the PSR, is the T_2 of the free water pool, and ω_{1CWPE} is the average power of the saturation pulse. The saturation rate of the longitudinal magnetization of the macromolecular pool, is described by a super-Lorentzian model, as described in work by Henkelman and colleagues[34,35].
   5. To analyze the DTI data, first use an affine transformation algorithm[36] to register each diffusion-weighted image to the corresponding non-diffusion weighted image. Then, for each pixel, measure the values for S in the non-diffusion weighted image and in each diffusion-weighted direction. Form a matrix composed of the diffusion encoding directions. Using multivariate, weighted least squares regression, regress the signal data on the diffusion encoding matrix and form **D**. Diagonalize **D** and perform a magnitude-sorting of the eigenvalues and their eigenvectors. Then calculate the mean diffusivity (MD) as:
   $$MD = \frac{\lambda_1 + \lambda_2 + \lambda_3}{3} \quad [6]$$
   where λ_1, λ_2, and λ_3 are the eigenvalues of the diffusion tensor. Also calculate the fractional anisotropy (FA) as:
   $$FA = \sqrt{\frac{3}{2}}\frac{\sqrt{(ADC - \lambda_1)^2 + (ADC - \lambda_2)^2 + (ADC - \lambda_3)^2}}{\sqrt{(\lambda_1^2 + \lambda_2^2 + \lambda_3^2)}} \quad [7]$$
   6. Analyze the FWMRI data using a quantitative approach that separates water and fat signals based on chemical shift (such as the FattyRiot algorithm, available for free download from https://github.com/welcheb/FattyRiot).

2. **Define Regions of Interest for Analysis**
   1. Specify ROIs on the anatomical images (by defining the boundaries of each muscle of interest). An example is shown in **Figure 1**.

2. Resize the ROIs to match the matrix size of the qMRI images. As necessary, adjust the alignment of the ROIs to match the qMRI map (for example, if the participant moved between acquisitions, a translation of the ROI position might be required to avoid overlapping the muscle boundaries).
3. Examine each ROI. If necessary, ensure that no pixels are included that contain partial volume artifacts, non-contractile tissue, and flow artifacts; please see **Figure 1** for examples.
4. Calculate the mean and standard deviation of the qMRI values in all pixels within the selected ROIs.

Representative Results

Figure 1 shows representative axial anatomical images acquired at the mid-thigh of a patient with polymyositis. Also shown is the location of the in-plane projection of the shim volume. Representative parameter maps for each qMRI method, all obtained from this same patient, are provided from **Figures 2 - 7.**

Figures 2A and **2B** show the ΔB_0 and nutation angle field maps, respectively. The B_0 field map demonstrates a strong spatial coincidence between its area of highest field homogeneity and the placement of the VOI for shimming, as indicated in **Figure 1A**. Within the muscles, the ΔB_0 values ranged from -40 to 52 Hz, with a mean of 9.3 Hz and a standard deviation of 11.2 Hz. In the nutation angle map, the values ranged from 84.7 to 122.3% of the nominal nutation angle. By comparing the nutation angle map with the structural images in **Figure 1**, it can be seen that the deviations from ideal nutation angle are more severe in the posterior muscles and are not obviously correlated to the presence of fat in a voxel.

Sample T_1 relaxometry data are presented in **Figure 3**. The images have been masked to exclude the subcutaneous fat and noise regions of the image. **Figure 3A** shows sample T_1 data and **Figure 3B** shows sample $T_{1,\mathrm{FS}}$ data. It is evident in **Figure 3A** that the T_1 of fat is considerably lower than that of muscle; therefore the T_1 values for muscle measured without using FS are lower than the $T_{1,FS}$ values. Also, the use of FS results in substantial loss of signal from regions of fat replacement or subcutaneous fat. Consequently, there are pixels in these image regions that are either devoid of fitted parameters, that represent residual water signals following FS, or in which the parameters are poorly estimated.

Figure 4A shows a masked parametric map of the $T_{2,\mathrm{FS}}$ values and **Figure 4B** shows the T_2 values. **Figure 4C** shows a sample T_2-dependent signal decay from a single pixel and the best fit of the data to a monoexponential model. A deviation from monoexponential relaxation behavior is noted. **Figure 4D** shows the results of NNLS analysis of these same signal data, with a single broad peak that likely includes both fat and water components.

Figures 5, 6, and **7** present examples of qMT, DTI and FWMRI data, respectively. For the qMT data, only the PSR is shown. The application of a signal threshold to these FS-data restricts curve-fitting to those voxels containing primarily muscle, resulting in dropout from the parameter map. Heterogeneity in the muscle values for PSR is also noted. Although the method also estimates the water T_2 and the exchange rate between the macromolecular and free water proton pools, these are not presented because the T_2 is better estimated using dedicated imaging sequences and because the exchange rate is both unreliably estimated and insensitive to pathology.

Figure 6A presents a parametric map of the MD, and **Figure 6B** presents a map of the FA values. MD values are elevated in blood vessels. Also, FA values are reduced in the regions corresponding to reduced PSR. As with other quantities, both the MD and the FA are inaccurately estimated in fat-replaced portions of muscle, where FS causes signal fallout. Also, FA is elevated outside of the shim volume. Lastly, a fat fraction map, calculated from the FWMRI data, is shown in **Figure 7**. These data quantify the qualitatively observed fat infiltration patterns noted in **Figure 1**. The corresponding water fraction map is simply equal to (1 - Fat) and is not shown.

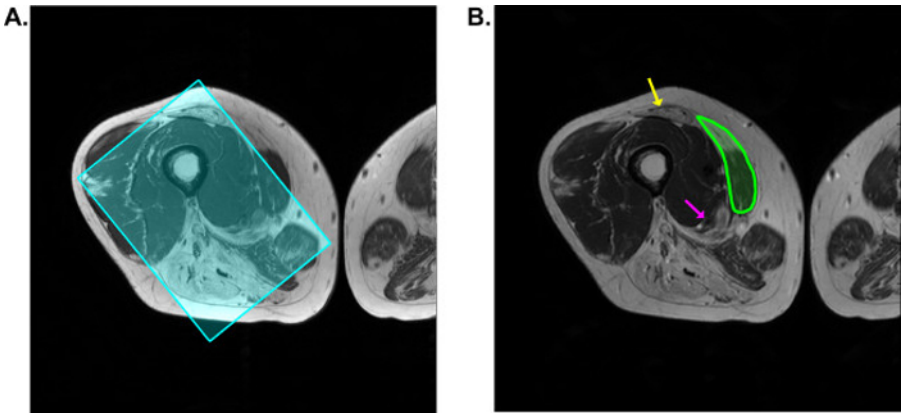

Figure 1: Sample Anatomical Images from a Patient with Polymyositis. All of the data shown in **Figures 2-7** were acquired at this slice position from this participant. **A.** T_1-weighted image, with the in-plane projection of the shim volume overlaid as the cyan-colored, semi-transparent rectangle. **B.** T_2-weighted image. Overlaid on the image in green is a sample ROI for the vastus medialis muscle. Through the semi-transparent ROI, areas of high signal, corresponding to fat replacement, are noted. The yellow arrow indicates an intramuscular tendon, and the magenta arrow indicates the region of the neurovascular bundle of the thigh. The images should be inspected for flow artifacts that may occur along the phase-encoding dimension and in line with the artery. Connective tissues such as fat and tendon are recommendation for exclusion from ROIs; also, if flow artifacts exist, they should be excluded. Please click here to view a larger version of this figure.

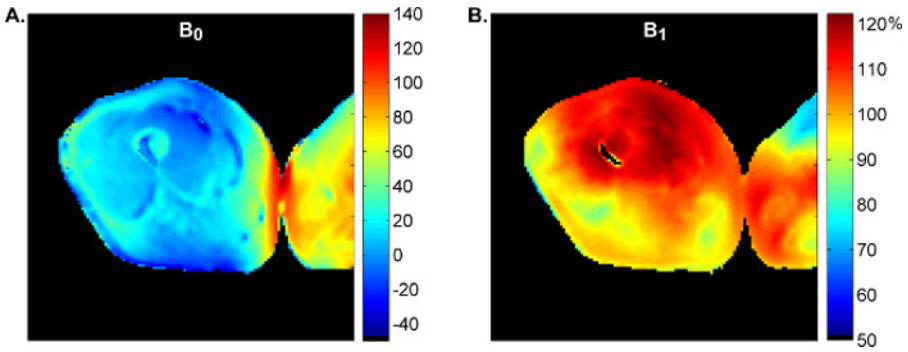

Figure 2: **ΔB_0 and Nutation Angle Maps, from the Same Patient Depicted in Figure 1. A.** ΔB_0 map, with the color scale indicating the deviation of the B_0 field from the center frequency in Hz. **B.** Nutation angle map, with the color scale indicating the percentage of the nominal nutation angle. Images have been masked to exclude the values from the noise regions of the image. Please click here to view a larger version of this figure.

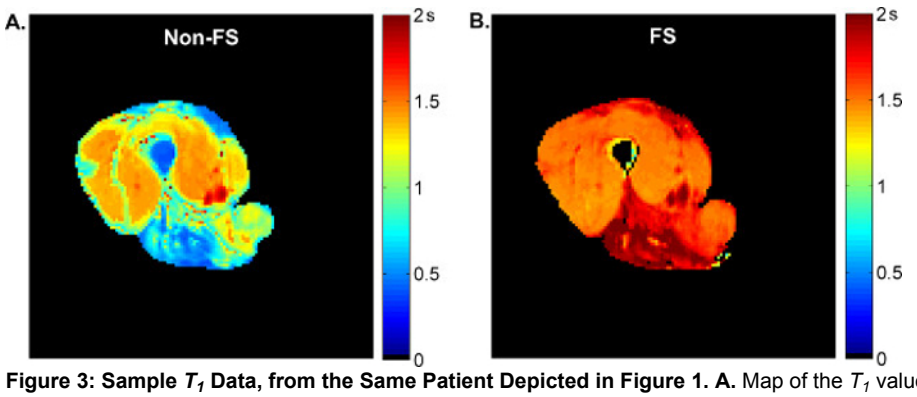

Figure 3: Sample T_1 Data, from the Same Patient Depicted in Figure 1. A. Map of the T_1 values, estimated by fitting the data to the inversion recovery with reduced pre-delay model. The color scale indicates the T_1 value in s. **B.** Map of the $T_{1,FS}$ values, estimated by fitting FS data to the same model. The color scale indicates the T_1 value in s. The images have been masked to exclude values from the subcutaneous fat, the contralateral leg, and the noise regions of the image. Note that the T_1 values are increased when fat signal suppression is used. Please click here to view a larger version of this figure.

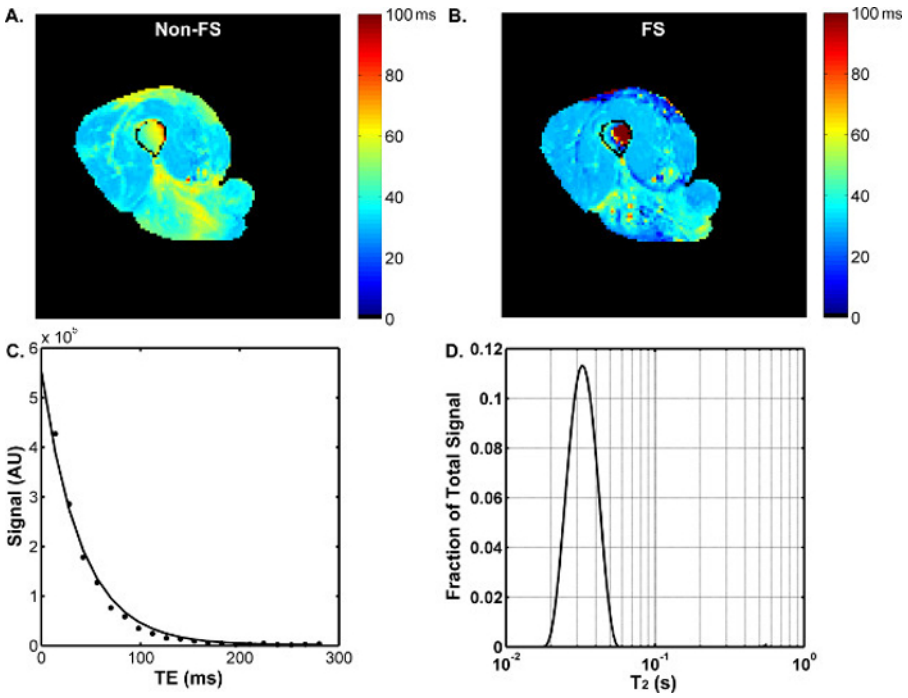

Figure 4: Sample T_2 Data, from the Same Patient Depicted in Figure 1. A. Map of the T_2 values, estimated by fitting the data to the monoexponential decay with noise term model. The color scale indicates the T_2 value in ms. **B.** Map of the $T_{2,FS}$ values, estimated by fitting the data to the same model. In **A** and **B**, the images have been masked to exclude values from the subcutaneous fat, the contralateral leg, and the noise regions of the image. **C.** Sample T_2 signal decay from a pixel in panel **C** and line of best fit to the monoexponential model (but note the deviation of the signal from the model, which indicates a non-monoexponential T_2). Abbreviation not previously noted: AU, arbitrary units. **D.** Non-negative least-squares analysis of the same raw signal decay data depicted in **C**. Please click here to view a larger version of this figure.

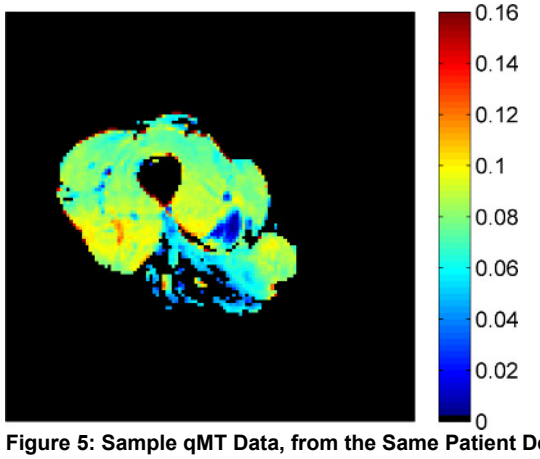

Figure 5: Sample qMT Data, from the Same Patient Depicted in Figure 1. The color scale indicates the PSR, a dimensionless quantity reflecting the ratio of macromolecular to free water protons. The use of FS methods results in substantial signal dropout from those regions of muscle that have been replaced by fat. Please click here to view a larger version of this figure.

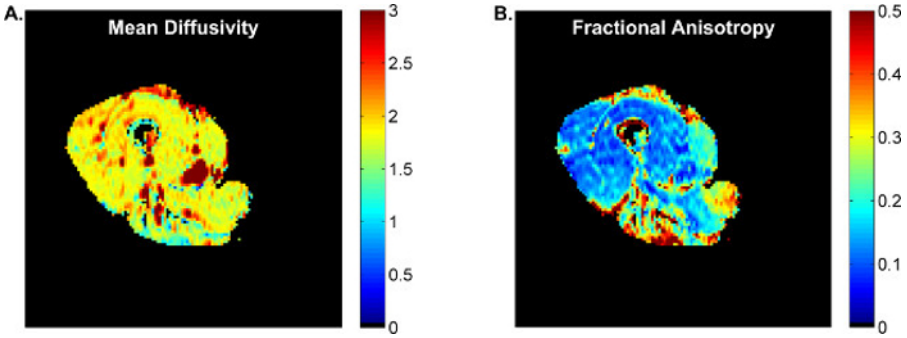

Figure 6: Sample Diffusion Data, from the Same Patient Depicted in Figure 1. Panel **A** shows the mean diffusivity, with the color scale indicating the diffusivity with units of 10^{-3} mm^2/s. Panel **B** shows the fractional anisotropy, which is a dimensionless quantity indicating the deviation of the diffusion system from purely isotropic diffusion. Please click here to view a larger version of this figure.

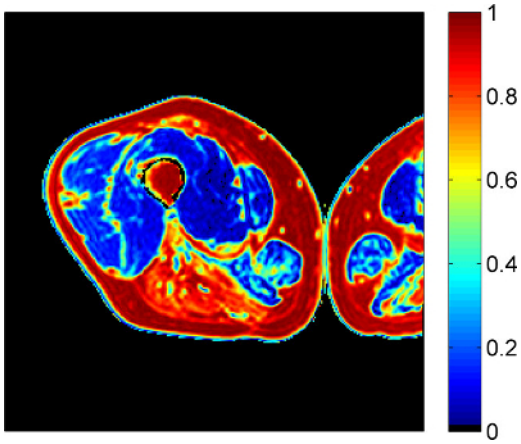

Figure 7: Sample FWMRI data, from the Same Patient Depicted in Figure 1. The color scale indicates the fat fraction; the corresponding water fraction map is simply (1 - Fat) and is not shown. Please click here to view a larger version of this figure.

Parameter		Localizers	T_1-Weighted	T_2-Weighted
General	Sequence type	2D, multi-slice, gradient-echo	2D, multi-slice, fast spin-echo	2D, multi-slice, fast spin-echo
	Preparation phases	Transmitter gain, receiver gain, center frequency, auto-shim	Receiver gain, center frequency, VOI shim	Receiver gain, center frequency, VOI shim
	Receive coil	Cardiac	Cardiac	Cardiac
	Number of excitations	1	1	1
	Total scan duration (min:sec)	1:23	1:40	0:54
Geometry	Anatomical plane(s)	Axial, coronal, and sagittal	Axial	Axial
	Number of slices/plane	20	11	11
	Slice thickness (mm)	10	7	7
	Inter-slice gap (mm)	0	0	0
	Slice acquisition order	Interleaved	Interleaved	Interleaved
	Acquired matrix	150 x 150	340 x 335	256 x 256
	Reconstructed matrix	512 x 512	512 x 512	512 x 512
	Field of view (mm)	450 x 450	256 x 256	256 x 256
	Reconstructed voxel size (mm)	0.88 x 0.88 x 10.00	0.50 x 0.50 x 7.00	0.50 x 0.50 x 7.00
Contrast	Repetition time (ms)	9	530	3000
	Effective echo time (ms)	7	6.2	100
	Echo spacing (ms)	N/A	6.2	11.8
	Excitation flip angle (°)	20	90	90
	Refocusing flip angle (°)	N/A	110	120
	RF shimming	Static	Adaptive	Adaptive
Signal acquisition	Readout type	Cartesian	Cartesian	Cartesian
	Parallel imaging	No	SENSE (g=1.4)	SENSE (g=2.0)
	Bandwidth/pixel (Hz/pixel)	1237.8	377.1	286.6

Table 1: Parameters used for Localizer Imaging and Structural Imaging. All sequences use the quadrature body coil for transmitting RF fields. Parameters such as TR, TE, echo spacing, and number of echoes can be adjusted slightly according to experimental needs while still maintaining T_1- and T_2- weighting. Abbreviation not previously noted: *g,* parallel imaging acceleration factor. Large field of view images are recommended, as they can be used to localize pathology and identify locations for qMRI sequences. The sagittal and coronal acquisitions are particularly helpful in this regard.

Parameter		Image Sequence	
		B_0-Mapping	**Flip Angle-Mapping**
General	Sequence type	3D, multiple RF-spoiled gradient-recalled echo	3D, fast gradient-echo, dual TR
	Preparation phases	Receiver gain, center frequency, VOI shim	Receiver gain, center frequency, VOI shim
	Receive coil	Quadrature-body	Cardiac
	Number of excitations	1	1
	Total scan duration (min:sec)	1:26	4:33
Geometry	Anatomical plane(s)	Axial	Axial
	Number of slices	11	55
	Slice thickness (mm)	7	7
	Inter-slice gap (mm)	0	0
	Acquired matrix	64 x 64 x 6	64 x 64 x 27
	Reconstructed matrix	128 x 128 x 11	128 x 128 x 55
	Field of view (mm)	256 x 256 x 77	256 x 256 x 385
	Reconstructed voxel size (mm)	2.00 x 2.00 x 7.00	2.00 x 2.00 x 7.00
Contrast	Repetition time (ms)	150	30.0, 130.0
	Echo time (ms)	{4,6, 6.9}	2.2
	Excitation flip angle (°)	25	60
	RF shimming	Adaptive	Adaptive
Signal acquisition	Readout type	Cartesian	Cartesian
	Bandwidth/pixel (Hz/pixel)	302.5	499.4

Table 2: Parameters used for ΔB_0 and Nutation Angle Mapping. Both sequences use the quadrature-body coil for transmitting the RF field; neither sequence uses parallel imaging.

Parameter		Image Sequence	
		T_1-Mapping	**T_2-Mapping**
General	Sequence type	3D, Inversion-recovery with gradient-spoiled, gradient-recalled echo readout	2D, single slice, multiple-spin-echo
	Preparation phases	Receiver gain, center frequency, VOI shim	Receiver gain, center frequency, VOI shim
	Number of excitations	1	2
	Total scan duration (min:sec)	1:44	12:04
Geometry	Anatomical plane(s)	Axial	Axial
	Number of slices	11	1
	Slice thickness (mm)	7	7
	Inter-slice gap (mm)	0	0
	Acquired matrix	128 x 128 x 6	128 x 128
	Reconstructed matrix	128 x 128 x 11	128 x 128
	Field of view (mm)	256 x 256 x 77	256 x 256
	Reconstructed voxel size (mm)	2.00 x 2.00 x 7.00	2.00 x 2.00 x 7.00
Contrast	Repetition time (ms)	Varied	4000
	Inversion pulse	180°, 1 ms, shape: block	N/A
	Inversion recovery times (ms)	50, 100, 200, 500, 1000, 2000, 6000	N/A
	Pre-delay time (ms)	1500	N/A
	Fat signal suppression (when used)	1331 binomial water-selective excitation	SPAIR (power: 2 µT, inversion delay 202 ms, frequency offset 250 Hz); Sinc-Gauss pre-pulse (90°, duration: 18 ms, frequency offset: 100 Hz)
	Excitation flip angle (°)	10	90
	Refocusing pulse	N/A	Version-S
	Echo time (ms)	N/A	{14, 28, 42…280}
	Number of echoes/ echo spacing (ms)	N/A	N/A
	RF shimming	Adaptive	Adaptive
Signal acquisition	Readout type	Cartesian	Cartesian
	Parallel imaging	SENSE (g=1.5)	SENSE (g=1.5)
	Bandwidth/pixel (Hz/pixel)	383	335.1

Table 3: Parameters used for T_1 and T_2 Mapping. T_1 and T_2 data are acquired with and without FS. Both sequences use the quadrature body coil for transmitting RF fields and a six-element cardiac coil for signal reception. The repetition time varies for the T_1-mapping sequence because it uses a fixed pre-delay time with variable inversion time.

Parameter		Image Sequence	
		qMT	**DTI**
General	Sequence type	3D, MT-weighted gradient-recalled echo	2D, multi slice, single-shot spin-echo EPI
	Preparation phases	Receiver gain, center frequency, VOI shim	Receiver gain, center frequency, VOI shim
	Number of excitations	2	6
	Total scan duration (min:sec)	10:41	6:28
Geometry	Anatomical plane(s)	Axial	Axial
	Number of slices	11	11
	Slice thickness (mm)	7	7
	Inter-slice gap (mm)	0	0
	Acquired matrix	128 x 128 x 6	64 x 64
	Reconstructed matrix	128 x 128 x1	128 x 128
	Field of view (mm)	256 x 256 x 77	256 x 256
	Reconstructed voxel size (mm)	2.00 x 2.00 x 7.00	2.00 x 2.00 x 7.00
Contrast	Repetition time (ms)	50	4,000
	MT pulse	Nominal flip angles: 360°, 820°; Pulse width: 20ms; Frequency offsets: 1, 2, 5, 10, 20, 50, 100 kHz	N/A
	Diffusion weighting (b) ($s \cdot mm^{-2}$)	N/A	b=450; 15 directions + one b=0 image
	Fat signal suppression (when used)	1331 binomial water-selective excitation	Gradient reversal; Sinc-Gauss pre-pulse (90°, duration: 18 ms, frequency offset: 100 Hz)
	Echo time (ms)	3.9	48
	Number of echoes/ echo spacing (ms)	N/A	N/A
	Excitation flip angle (°)	6	90
	RF shimming	Adaptive	Adaptive
Signal acquisition	Readout type	Cartesian	Cartesian
	Parallel imaging	SENSE (g=1.5)	SENSE (g=1.5)
	Bandwidth/pixel (Hz/pixel)	383	42.1

Table 4: Parameters used for qMT and DTI. Both sequences use the quadrature-body coil for transmitting the RF field and a six-element cardiac coil for signal reception. Abbreviation not previously noted: EPI, echo-planar imaging.

Parameter		Image Sequence
		FW-MRI
General	Sequence type	3D gradient-recalled echo
	Preparation phases	Receiver gain, center frequency, VOI shim
	RF transmission coil	Quandrature-body
	Receive coil	Cardiac
	Number of excitations	1
	Total scan duration (min:sec)	0:18
Geometry	Anatomical plane(s)	Axial
	Number of slices	11
	Slice thickness (mm)	7.0 mm
	Inter-slice gap (mm)	0 mm
	Acquired matrix	128 x 128 x 4
	Reconstructed matrix	128 x 128 x 7
	Field of view (mm)	256 x 256 x 77
	Reconstructed voxel size (mm)	2.00 x 2.00 x 7.00
Contrast	Repetition time (ms)	75
	Excitation flip angle (°)	22
	Echo times (ms)	{1.34, 2.87, 4.40, 5.93…8.99}
	Excitation flip angle (°)	6
	RF shimming	Adaptive
Signal acquisition	Readout type	Cartesian
	Parallel imaging	SENSE (g=1.3)
	Bandwidth/pixel (Hz/pixel)	1395.1

Table 5: Parameters used for FW-MRI.

Discussion

Muscle diseases such as the muscular dystrophies and idiopathic inflammatory myopathies constitute of group of diseases that are heterogeneous in etiology and, as individual entities, rare in their incidence. For example, Duchenne muscular dystrophy — the most common form of muscular dystrophy — has an incidence of 1 in 3,500 live male births[37,38]; dermatomyositis, to which this protocol has been applied, has an incidence of 1 in 100,000[39]. The higher collective incidence of these diseases, however, and their often overlapping pathological signs — atrophy, inflammation, fat infiltration, membrane damage, and fibrosis — support the development and application of a common set of methods for quantitatively characterizing these diseases.

QMRI is able to characterize many of these pathophysiological changes non-invasively. As with any scientific method, qMRI studies must be implemented in a careful manner. A fundamental issue is safety. Also, each qMRI method described here has associated sources of error; and for obvious reasons, it is important to understand and recognize these errors. Lastly, many of the measurements have a complex interpretation. These issues are discussed here. In presenting the Discussion, we note that the protocol presented here describes what we feel is the best experimental approach for our purposes. We recognize that others may have differing views, additional knowledge, or may choose to weigh the potential outcomes of protocol optimization differently than we have. Also, the reader's MRI system may not have all of the options described in the protocol available; or the reader may have additional options that are not available on our system. We have noted which aspects of our protocol have been custom-programmed on our system. The reader is advised to consider all of the literature completely, examine all relevant options on his/her system, and make decisions that result in the best possible protocol for his/her experimental aims.

MRI Safety Issues

MRI uses several types of magnetic fields. The B_0 field strength of the system used in the studies described here is 3.0 Tesla, or approximately 15,000 times the Earth's field of ~ 0.2 mT. Pulsed RF magnetic fields (B_1) are used to introduce energy into the spin system and create the resonance phenomenon. Gradient magnetic fields are turned on and off during the imaging sequence and are used for several purposes. They are used to create a linear relationship between NMR frequency and spatial position for the purpose of spatial encoding and are also used to eliminate unwanted sources of signals.

Each of these types of magnetic fields has safety concerns associated with it. A major safety concern associated with the B_0 field is the acceleration of magnetic objects toward the magnet. The B_0 field is always present. Because the strength of a magnetic field varies as a function of $1/d^3$, where d is the distance from the source of the field, the B_0 field increases rapidly as one approaches the MRI system. Ferromagnetic objects can be accelerated toward the MRI system with little or no warning and can cause severe injury or death. Therefore, they must be

removed and secured outside of the MRI room. Other hazards associated with the B_0 field are the placement of abnormal torques on implanted magnetic objects and erasure or other damage to magnetically sensitive devices. B_1 fields can heat tissues, and this effect may be enhanced in the areas around implanted metal objects. Gradient fields can induce electrical currents in conductive objects (such as nerves and implanted medical devices). The switching of gradient fields also generates potentially loud and unpleasant acoustic noise. Government regulatory agencies have placed strict limits on the levels and durations of exposure to these various types of magnetic fields, and human imaging systems have intrinsic software controls that ensure compliance with these guidelines.

The reader should know that this presentation is somewhat cursory. It is incumbent upon all personnel associated with MRI testing to be fully aware of all relevant safety issues and how to prevent accidents. Also, all personnel associated with MRI testing should be screened for potentially hazardous implanted metals or medical devices.

Pre-testing Lifestyle Restrictions

Exerting as much experimental control over pre-testing lifestyle behaviors as possible is an important component of this protocol. The case of T_2 measurements is provided as an example of why this control is needed. T_2 is considered a leading MRI biomarker of neuromuscular disease[40]. However, the muscle water proton T_2 can be elevated for several reasons. In qMRI studies for neuromuscular diseases, the T_2 measured in the presence of FS is generally presumed to reflect a state of chronic inflammation related to disease severity, while the non-FS T_2 can also reflect fat infiltration. However, T_2 can also undergo medium-term elevations because of eccentric exercise[41], which may affect patients and healthy subjects differently[42]. For this reason, the authors recommend restricting moderate or heavy exercise for 48 hours prior to testing. T_2 can also undergo shorter-lived elevations as a result of acute bouts of exercise[43,44]. For a patient with severe muscle loss, walking could constitute exercise intense enough to elevate T_2. For this reason, the authors recommend that on the day of testing, patients be transported over long distances using an MRI-compatible wheelchair.

Data Acquisition and Analysis: General Issues

An important point is that careful pilot testing, first in healthy persons and then in persons with the disease of interest, is essential. Many experimental options are highly specific to the MRI system (including but not limited to B_0 field strength, shimming strategies, RF coil options, maximum magnetic field gradient strength, and the availability of advanced options such as RF pulse shape). Sequence-specific pilot testing goals are described below. Other issues that affect data quality are biological in nature, such as the type of disease and the expected types of pathology, age of the patient population, and even the body part to be imaged. All of these factors should be considered during pilot testing.

During data acquisition itself, a frequently encountered problem is motion. The imaging portion of the protocol presented here can require as much as one hour. Some of the sequences (such as echo-planar imaging) are insensitive to bulk motion; but other sequences are long, require exact image alignment for accurate parameter estimation, and/or have signals that are intrinsically motion-sensitive. As noted in the protocol, taking steps to instruct the participant and promote his/her comfort is an important way to prevent both voluntary and involuntary movements. Another strategy is to limit motion with padding and gently, but effectively, placed straps that attach to the patient bed. Image registration techniques are available for post-processing; because muscles are easily deformable organs, non-rigid registration techniques are often required. Non-rigid registration will always be required for diffusion imaging methods based on echo-planar imaging. Despite the general usefulness of image registration techniques, any method for preventing motion or reducing artifacts will be superior to solutions that require extensive post-processing. Defining the best available motion-reduction strategy in the subject population of interest should be a goal for pilot testing.

Good reproducibility requires consistency of slice placement. In the protocol steps, we describe referencing the slice position to reproducible anatomical landmarks. An effective strategy for this in the thigh is to obtain coronal images of the entire thigh, permitting visualization of the entire femur. The image analysis tools on the MRI system typically include a digital ruler function. This can be used to measure a specific point (such as the midpoint) of the head of the femur and the femoral condyles, and place the center position of the slice stack there. This procedure is illustrated in the video.

Inhomogeneous B_0 and B_1 fields are unavoidable problems in MRI, but strategies exist for reducing the levels of inhomogeneity. A fundamental strategy is to locate the body part to be imaged at or near the magnet's center. The protocol presented here includes the B_0 shimming routines that, in the authors' experience, are most effective for these experimental conditions. Because the participant may move during the protocol, B_0 shimming is repeated as part of the calibration steps for every sequence. Also, many of the acquisitions use parallel imaging techniques to accelerate signal acquisition and thereby reduce the ΔB_0-dependent differences in phase evolution that cause image distortions. Because the RF transmit coil employed in these studies contain two coil elements, B_1 shimming methods can be used and are described in the protocol. In addition, the protocol includes ΔB_0 and nutation angle field mapping sequences for real-time quality control. The protocol described above includes the tolerances in ΔB_0 and nutation angle that are acceptable for the experimental conditions, RF pulse shapes, and gradient spoiling schemes described here. These were determined in pilot testing and re-emphasize the value of careful protocol development.

In practice, there may be a limited number of strategies available in real-time to affect the B_0 and B_1 fields' homogeneities, while maintaining the methodological consistency that is necessary for good experimental design. Users are therefore advised to investigate all options available to them with thorough pilot testing, ultimately arriving at effective and generally applicable strategies for the subject population of interest. B_0 shimming options include iterative methods that minimize a parameter such as the water peak's line-width at half-maximum peak height and methods that calculate the optimum shim channel settings using a ΔB_0 map. The former methods can be based on a non-localized acquisition or, as in the protocol described here, the acquisition of signal from a localized volume. The goals for pilot testing of B_0 shimming options include the best general strategy (iterative vs. image-based) as well as the particulars of how best to define the region of interest for shimming. The reader may wish to consider factors such as the size and orientation of the volume of interest, the relative amounts of muscle and fat to include in the shimming volume, and how beyond the slice stack to shim. It is worthwhile to examine the within-slice projection of the shim volume in each slice to be imaged.

In the case of the B_1 field, the type of RF coils used for transmission and reception and the types of RF pulses used are important determinants of field homogeneity. The protocols described in the tables include the RF pulse parameters that we have found optimal for our experimental conditions. Regarding coil selection, the protocol described here combines separate volume transmission and receive-only volume coils. The transmission coil is the quadrature-body coil that is built into the system, and creates a relatively homogeneous B_1 field across a large anatomical

region. Depending on the anatomical region to be studied, there may be a variety of receive coil options; in our case, pilot testing showed the six-element, phased array cardiac coil to be the best available solution. Other options available include surface coils and combination transmission/receive volume coils. Surface coils are limited in depth of penetration of the B_1 field and we do not generally recommend their use for imaging applications. Combination transmission/receive volume coils may offer better signal-to-noise ratio (SNR) performance and B_1 homogeneity than a built-in quadrature-body coil, but are not available for all anatomical regions. A final comment is that when phased-array coils are available, they permit the use of parallel imaging techniques that speed up acquisition and reduce spatial distortions in techniques such as echo-planar imaging. These gains come with an SNR penalty, however, and so pilot testing should be directed toward finding the solution that provides best overall image quality.

But because these strategies do not completely compensate for inhomogeneous B_0 and B_1 fields, another use of ΔB_0 and nutation angle field maps is in post-processing. These maps can be used to improve the calculation of some quantitative parameters or to correct image distortions. But some ΔB_0- and B_1-related problems may not be fully or even partly correctable in post-processing. Some examples include reduced efficacy of FS methods, gross image distortions in techniques such as echo-planar imaging, low signal, poor refocusing efficiency in T_2 measurements or FSE methods, and poor inversion efficiency in T_1 measurements. Again, rigorous pilot testing and real-time quality control steps are essential.

Many of the sequences use fat-signal suppression or water-selective excitation as a mechanism for avoiding muscle signal contamination by fat and/or for reducing the existence of artifacts caused by the different resonance frequencies of water and lipid protons. When FS is used, a combination of up to three methods is employed. The aliphatic signals are reduced or eliminated using a spectrally selective adiabatic inversion recovery (SPAIR) pulse, which selectively inverts these signals. As the signal recovers from a signal value of $-M_0$ toward $+M_0$, there is a time at which the net signal equals zero. The imaging data are acquired at this signal nulling point. It should be noted that this time point depends on parameters such as the repetition time and the number of slices, and so must be optimized separately for each sequence during the pilot testing process. Also, the bandwidth of the SPAIR pulse should be only wide enough to eliminate fat signals, so that the reduction of water signal amplitude is kept to a minimum. Taking steps to maximize B_0 uniformity will be helpful in this regard. Many of the sequences also use a saturation pulse on the olefinic proton resonance[45]; this pulse is applied immediately prior to the imaging sequence. Where possible, a gradient reversal technique is used. In this method, the sign of the slice selection gradient is reversed between the slice selection and refocusing pulses; this causes signals far off-resonance from water not to be refocused. An additional advantage of this approach is that unlike RF-based methods, gradient reversal does not allow fat signals to recover by longitudinal relaxation during the RF pulse train. Additional strategies, such as Dixon-based methods[46], are also available.

A common issue in data analysis is whether to use mean ROI signal analyses (in which the signals in an ROI are averaged and then fitted to a model) or pixel-based analyses (in which the model fitting occurs on a pixel-by-pixel basis, and statistics are then calculated for the fitted parameters). The advantage of the former method is that signal averaging improves the effective SNR. If the intrinsic SNR is low, then this strategy may help to avoid the parameter-biasing effects of the noise floor. The advantage of the latter approach is that spatial heterogeneity is a common pathological feature of neuromuscular disorders. By fitting the values on a pixel-by-pixel basis, this heterogeneity can be appreciated and used to characterize additional aspects of disease phenotype. If the SNR permits this type of analysis to be performed validly, the authors recommend this approach. Recent work by Willcocks and colleagues illustrates the value of this approach in monitoring disease progression[47].

Data Acquisition and Analysis: Imaging Sequence-specific Issues

The protocol uses inversion recovery methods for a robust measurement of T_1. A practical limitation of many implementations of the inversion recovery sequence is a long total scan time. The sequence used in this protocol uses a three-dimensional, Fast, Low-Angle Shot (FLASH) readout, a modest amount of parallel imaging acceleration, and a reduced pre-sequence delay to decrease the total scan time to less than two minutes. Seven inversion times are sampled, spaced in an approximately geometric progression from 50 to 6,000 ms. This strategy samples the inversion-recovery signal curve most frequently during those portions of the signal recovery when the time derivative of the signal is highest. The sequence is repeated with and without FS because inflammation and fat infiltration have confounding effects on the overall proton T_1: inflammation increases the water T_1, while fat has a lower T_1 than water. Thus measuring both T_1 and $T_{1,FS}$ aids in the interpretation of the data because it allows one to resolve between these opposing influences of fat infiltration and inflammation on T_1. Parameter estimation is accomplished by using non-linear, least square regression methods in a scientific computing software package.

The T_2 measurements are conducted under FS and non-FS conditions as well, and for an analogous reason: inflammation and fat each can increase the T_2. In addition to inflammation, pathologic processes such as Z-disc streaming and losses to membrane integrity would also be expected to influence the water T_2 values. Although the measurement of both T_2 and $T_{2,FS}$ cannot distinguish among all of these sources of pathology, this practice does afford increased interpretability to the data by resolving between general and muscle tissue-specific pathology. An alternative strategy to measuring a water-only T_2 value is to use ^{1}H MR spectroscopy to separate water from lipids on the chemical shift axis of the spectrum. Although this approach has significantly lower spatial resolution than imaging and may be subject to user discretion and subjectivity regarding volume placement during data acquisition, it provides an unambiguous way to separate water and lipid signals.

The protocol for T_2 measurement presented here employs several methods to mitigate some common sources of error in T_2 measurements, namely B_1 inhomogeneity and stimulated echo formation from imperfect refocusing pulses. Stimulated echoes are formed by any combination of three non-180° pulses. Given that some level of B_1 inhomogeneity always exists, and that multi-echo trains are used to sample the T_2-dependent signal decay, stimulated echoes are a potentially significant source of error in T_2 measurements. The strategies used here to eliminate stimulated echo formation include the use of a single slice acquisition, an optimized sequence of spoiler gradients before and after the refocusing pulses[48], linear echo spacing[49], and the use of the B_1-insensitive "Version-S" composite refocusing pulse[50], which significantly reduces the artifacts caused by imperfect refocusing and while still providing a sufficient bandwidth for refocusing both water and lipid signals. In pilot testing, we observed that the optimized spoiling scheme and the Version-S pulse significantly reduced the appearance of stimulated echoes. We note that both of these objects have been programmed specifically on our system. The Version-S pulse does increase the specific absorption rate (SAR) of RF energy; thus a long TR and larger inter-echo spacing are required to remain within the safety limits for SAR. However, the authors' experience is that well coached, comfortable patients can remain sufficiently still during the ~12 min. total scan time. Also, the inter-echo spacing value of 14 ms is sufficient to detect multi-exponential relaxation, when it exists. An alternate approach, not employed here, is to include refocusing pulse efficiency and stimulated echoes into the fitting[38,28], which will provide a B_1 map and permit multi-slice acquisitions[39]. The

reader is also referred to several recent papers describing the implementation and interpretation of T_2 measurements in muscle disease, which provide some similar and some different recommendations concerning these methods[40,51].

The protocol presented here uses the pulsed saturation method for qMT imaging. Although there are five fitted parameters that are generated, only the PSR is reported. This is because the other four parameters are either better estimated by using other methods (such as the T_2 of the free water pool) or lack pathological sensitivity (such as the exchange rate between pools[52,53]). Compared with other qMT methods, 3D coverage can be achieved within a clinically feasible time for the pulse saturation method. Another advantage to this qMT approach is its compatibility with the spatial-spectral binomial pulse methods for water-selective excitation, which was found to suppress > 95% fat signals throughout the image. Both the water-selective excitation pulse and the off-resonance saturation pulses have been customized on our system. Previous numerical simulations[54] have indicated that an additional fat component to the signal may bias qMT parameter estimates; thus FS is always recommended for qMT imaging in skeletal muscles. As discussed above, excessive B_1 inhomogeneity and motion artifacts can bias qMT parameter estimates as well.

The DT-MRI protocol is implemented with attention to spatial distortions in echo-planar imaging, SNR, and *b*-value. Here, spatial distortions are reduced by using parallel imaging, and corrected in post-processing by using an affine registration. As noted in previous works, the SNR and *b*-value have interactive effects on the estimation of **D**[55-57], with low SNR values resulting in particularly erroneous estimation of λ_1, λ_3, $\mathbf{v}_1$, and FA[55,57-59]. In muscle, the SNR requirements for accurate tensor estimation are lowest in the range b=435-725 s/mm^2 [55-57,60]. Although other authors[61,62] have reported favorable results from using denoising approaches for muscle DT-MRI, the large ROIs analyzed in this protocol have sufficient signal averaging so as not to require these additional steps. The reader is referred to several reviews of the topic of optimal implementation of DT-MRI methods[56,63].

Lastly, some caveats and possible sources of error related to quantitative FWMRI are noted. First, the FattyRiot fitting algorithm adopted here assumes a specific fat spectrum with nine peaks at fixed locations and relative amplitudes[64]. The assumed fat spectrum is not a perfect match to the true *in vivo* spectrum, which will vary subject to subject; however, solving for an arbitrary fat spectrum is not practical with a small number of echoes. Second, the algorithm fits for a single R_2* decay factor shared by both water and fat signals. It is known that completely ignoring R_2* confounds quantitative fat signal fraction measurements, and that fitting for a single R_2* decay is adequate[65]. However, the exact R_2* of the water and individual fat peaks varies. Third, FWMRI separation algorithms using complex images are vulnerable to severe B_0 field inhomogeneity that can cause misclassification of fat and water signals. In addition to using robust spatially constrained algorithms, a smaller echo spacing allows capturing larger B_0 field variations. Algorithms using magnitude images are more robust in the presence of B_0 field inhomogeneity, but they suffer SNR penalties. Algorithms using complex images may also be confounded by eddy currents or any other time-varying phase effect. Such confounding phase effects are typically worst for the first echo in a multiple echo readout train and can be mitigated by simply ignoring such echoes. Alternatively, a mixed magnitude and complex signal model can be adopted[66]. Users of FWMRI algorithms that take complex images as input should avoid other sources of potential perturbation of the complex images such as corrections applied in the image reconstruction pipeline on many commercial MRI scanners. Such phase corrections should be deactivated, or the user should reconstruct images directly from the original raw data. Finally, any estimation of fat fraction using FWMRI is actually an estimation of fat signal fraction, and thus is influenced by any factor that differentially scales the fat or water signals. The T_1 is the primary factor affecting fat and water signal levels in a typical gradient echo scan. T_1-weighting is a function of T_1, TR, and excitation nutation angle. T_1 bias in fat signal fraction estimates is worst for voxels with a nearly equal mix of water and fat. Increasing the TR or reducing the nutation angle can minimize the bias. T_1 bias can also be corrected retrospectively using assumed T_1 values for water and fat, as we do here (1.4 s and 0.3 s for water and fat, respectively), or measured values.

Protocol Formation/Sequence Selection

As discussed above, the muscle pathologic landscape is a complex one. FWMRI is unique among the measurements in this protocol in that it has an unambiguous interpretation. As noted, many of the other qMRI biomarkers measured here have a non-specific pathological basis that often includes edema but may also include fat infiltration, fibrosis, membrane damage, and sarcomeric disruption. It is emphasized that some of these sensitivities are still just hypothesized to exist. There is a considerable amount of work that needs to be done in order to demonstrate, quantitatively, the relative importance of these and other pathologic processes or states to each qMRI biomarker. With such understanding, the multi-parametric approach described here may allow, through the combination of variables, more specific descriptions of individual pathologies.

Alternatively, the reader may elect to adapt this protocol by selecting a subset of the measurements presented here. For example, the added value of FS and non-FS measurements is probably low in conditions not characterized by fat replacement of muscle. This could allow for reduced imaging time for the patient, additional measurements to be made (such as MR spectroscopy, MRI perfusion imaging, *etc.*), or additional body parts to be imaged. As many muscle diseases present in a proximal-to-distal fashion, the protocol described here is implemented in the thighs, as disease in this region may provide an early marker of disease involvement. However, measuring pathology in both proximal and distal regions may allow improved measures of disease progression.

Conclusions

In conclusion, this qMRI protocol allows the quantitative assessment of edema, fat infiltration, and atrophy, which are three major pathologic components of neuromuscular disorders. By incorporating a broad collection of measurements (T_1, T_2, diffusion, qMT, FWMRI), the interpretability of the data is both broadened and deepened. When careful attention is paid to potential sources of error, this approach can accurately and precisely characterize several major components of neuromuscular disease.

p.p1 {margin: 0.0px 0.0px 0.0px 0.0px; font: 14.0px Helvetica; color: #3a3a3a} span.s1 {font: 11.0px Helvetica}

Disclosures

None of the authors has a financial conflict of interest to report.

Acknowledgements

We acknowledge grant support from the National Institutes of Health: NIH/NIAMS R01 AR050101 (BMD), NIH/NIAMS R01 AR057091 (BMD/JHP), NIH/NIBEB K25 EB013659 (RDD), and the Vanderbilt CTSA award RR024975. We also thank the reviewers for the comments and the subject for participating in these studies.

References

1. Wokke, B. H. *et al.* Comparison of Dixon and T_1-weighted MR methods to assess the degree of fat infiltration in duchenne muscular dystrophy patients. *J Magn Reson Imaging.* **38** (3), 619-624 (2013).
2. Carr, H., & Purcell, E. Effects of diffusion on free precession in NMR experiments. *Phys Rev.* **94**, 630-638 (1954).
3. Whittall, K. P., & MacKay, A. L. Quantitative interpretation of NMR relaxation data. *Journal of Magnetic Resonance.* **84** (1), 134-152 (1989).
4. Park, J. H. *et al.* Dermatomyositis: correlative MR imaging and P-31 MR spectroscopy for quantitative characterization of inflammatory disease. *Radiology.* **177** (2), 473-479 (1990).
5. Park, J. H. *et al.* Magnetic resonance imaging and p-31 magnetic resonance spectroscopy provide unique quantitative data useful in the longitudinal management of patients with dermatomyositis. *Arthritis & Rheumatism.* **37** (5), 736-746 (1994).
6. Park, J. H. *et al.* Use of magnetic resonance imaging and p-31 magnetic resonance spectroscopy to detect and quantify muscle dysfunction in the amyopathic and myopathic variants of dermatomyositis. *Arthritis & Rheumatism.* **38** (1), 68-77 (1995).
7. Huang, Y. *et al.* Quantitative MR relaxometry study of muscle composition and function in Duchenne muscular dystrophy. *J Magn Reson Imaging.* **4** (1), 59-64 (1994).
8. Kim, H. K. *et al.* T_2 mapping in Duchenne muscular dystrophy: distribution of disease activity and correlation with clinical assessments. *Radiology.* **255** (3), 899-908 (2010).
9. Arpan, I. *et al.* T_2 mapping provides multiple approaches for the characterization of muscle involvement in neuromuscular diseases: a cross-sectional study of lower leg muscles in 5-15-year-old boys with Duchenne muscular dystrophy. *NMR in Biomedicine.* **26** (3), 320-328 (2013).
10. Fan, R. H., & Does, M. D. Compartmental relaxation and diffusion tensor imaging measurements in vivo in λ-carrageenan-induced edema in rat skeletal muscle. *NMR in Biomedicine.* **21** (6), 566-573 (2008).
11. Sled, J. G., & Pike, G. B. Quantitative interpretation of magnetization transfer in spoiled gradient echo MRI sequences. *J Magn Reson.* **145** (1), 24-36 (2000).
12. Gochberg, D. F., & Gore, J. C. Quantitative magnetization transfer imaging via selective inversion recovery with short repetition times. *Magn Reson Med.* **57** (2), 437-441 (2007).
13. Li, K. *et al.* Optimized inversion recovery sequences for quantitative T1 and magnetization transfer imaging. *Magn Reson Med.* **64** (2), 491-500 (2010).
14. Louie, E. A., Gochberg, D. F., Does, M. D., & Damon, B. M. Magnetization transfer and T2 measurements of isolated muscle: effect of pH. *Magn Reson Med.* **61** (3), 560-569 (2009).
15. Sinclair, C. D. J. *et al.* Quantitative magnetization transfer in in vivo healthy human skeletal muscle at 3 T. *Magn Reson Med.* **64** (6), 1739-1748 (2010).
16. Sinclair, C. *et al.* Multi-parameter quantitation of coincident fat and water skeletal muscle pathology. *Proc 21st Ann Meeting ISMRM.* (2013).
17. Bryant, N. *et al.* Multi-parametric MRI characterization of inflammation in murine skeletal muscle. *NMR Biomed.* **27** (6), 716-725 (2014).
18. Aisen, A. M., Doi, K., & Swanson, S. D. Detection of liver fibrosis with magnetic cross-relaxation. *Magn Reson Med.* **31** (5), 551-556 (1994).
19. Kim, H. *et al.* Induced hepatic fibrosis in rats: hepatic steatosis, macromolecule content, perfusion parameters, and their correlations-preliminary MR imaging in rats. *Radiology.* **247** (3), 696-705 (2008).
20. Basser, P. J., Mattiello, J., & LeBihan, D. MR diffusion tensor spectroscopy and imaging. *Biophys J.* **66** (1), 259-267 (1994).
21. Heemskerk, A., Strijkers, G., Drost, M., van Bochove, G., & Nicolay, K. Skeletal muscle degeneration and regeneration following femoral artery ligation in the mouse: diffusion tensor imaging monitoring. *Radiology.* **243** (2), 413-421 (2007).
22. Zaraiskaya, T., Kumbhare, D., & Noseworthy, M. D. Diffusion tensor imaging in evaluation of human skeletal muscle injury. *J Magn Reson Imaging.* **24** (2), 402-408 (2006).
23. Qi, J., Olsen, N. J., Price, R. R., Winston, J. A., & Park, J. H. Diffusion-weighted imaging of inflammatory myopathies: polymyositis and dermatomyositis. *J Magn Reson Imaging.* **27** (1), 212-217 (2008).
24. McMillan, A. B., Shi, D., Pratt, S. J., & Lovering, R. M. Diffusion tensor MRI to assess damage in healthy and dystrophic skeletal muscle after lengthening contractions. *J Biomed Biotech.* **2011**, 970726 (2011).
25. Scheel, M. *et al.* Fiber type characterization in skeletal muscle by diffusion tensor imaging. *NMR Biomed.* **26** (10), 1220-1224 (2013).
26. Kaufman, L. D., Gruber, B. L., Gerstman, D. P., & Kaell, A. T. Preliminary observations on the role of magnetic resonance imaging for polymyositis and dermatomyositis. *Annalsrheumatic Dis.* **46** (8), 569-572 (1987).
27. Dixon, W. T. Simple proton spectroscopic imaging. *Radiology.* **153** (1), 189-194 (1984).
28. Glover, G. H. Multipoint Dixon technique for water and fat proton and susceptibility imaging. *J Magn Reson Imaging.* **1** (5), 521-530 (1991).
29. Berglund, J., & Kullberg, J. Three-dimensional water/fat separation and T2* estimation based on whole-image optimization--application in breathhold liver imaging at 1.5 T. *Magn Reson Med.* **67** (6), 1684-1693 (2012).
30. Gloor, M. *et al.* Quantification of fat infiltration in oculopharyngeal muscular dystrophy: Comparison of three MR imaging methods. *J Magn Reson Imaging.* **33** (1), 203-210 (2011).
31. Fischmann, A. *et al.* Quantitative MRI and loss of free ambulation in Duchenne muscular dystrophy. *J Neurol.* **260** (4), 969-974 (2013).
32. Li, K. *et al.* Multi-parametric MRI characterization of healthy human thigh muscles at 3.0 T - relaxation, magnetization transfer, fat/water, and diffusion tensor imaging. *NMR Biomed.* **27** (9), 1070-1084 (2014).
33. Does, M. *Multi-Exponential Relaxation Analysis (MERA) Toolbox, Version 2.*, <http://www.vuiis.vanderbilt.edu/~doesmd/MERA/MERA_Toolbox.html> (2014).
34. Morrison, C., Stanisz, G., & Henkelman, R. M. Modeling magnetization transfer for biological-like systems using a semi-solid pool with a super-Lorentzian lineshape and dipolar reservoir. *J Magn Reson Series B.* **108** (2), 103-113 (1995).

Copyright © 2016 Journal of Visualized Experiments

35. Li, J. G., Graham, S. J., & Henkelman, R. M. A flexible magnetization transfer line shape derived from tissue experimental data. *Magn Reson Med.* **37** (6), 866-871 (1997).
36. Mangin, J. F., Poupon, C., Clark, C., Le Bihan, D., & Bloch, I. Distortion correction and robust tensor estimation for MR diffusion imaging. *Med Image Anal.* **6** (3), 191-198 (2002).
37. Moser, H. Duchenne muscular dystrophy: pathogenetic aspects and genetic prevention. *Hum Genet.* **66** (1), 17-40 (1984).
38. van Essen, A. J., Busch, H. F., te Meerman, G. J., & ten Kate, L. P. Birth and population prevalence of Duchenne muscular dystrophy in The Netherlands. *Hum Genet.* **88** (3), 258-266 (1992).
39. Bendewald, M. J., Wetter, D. A., Li, X., & Davis, M. P. Incidence of dermatomyositis and clinically amyopathic dermatomyositis: A population-based study in olmsted county, minnesota. *Arch Dermatol.* **146** (1), 26-30 (2010).
40. Carlier, P. G. Global T2 versus water T_2 in NMR imaging of fatty infiltrated muscles: different methodology, different information and different implications. *Neuromuscul Disord.* **24** (5), 390-392 (2014).
41. Foley, J. M., Jayaraman, R. C., Prior, B. M., Pivarnik, J. M., & Meyer, R. A. MR measurements of muscle damage and adaptation after eccentric exercise. *J Appl Physiol.* **87** (6), 2311-2318 (1999).
42. Garrood, P. *et al.* MR imaging in Duchenne muscular dystrophy: quantification of T1-weighted signal, contrast uptake, and the effects of exercise. *J Magn Reson Imaging.* **30** (5), 1130-1138 (2009).
43. Bratton, C. B., Hopkins, A. L., & Weinberg, J. W. Nuclear magnetic resonance studies of living muscle. *Science.* **147**, 738-739 (1965).
44. Fleckenstein, J. L., Canby, R. C., Parkey, R. W., & Peshock, R. M. Acute effects of exercise on MR imaging of skeletal muscle in normal volunteers. *AJR Am J Roentgenol.* **151** (2), 231-237 (1988).
45. Williams, S., Heemskerk, A., Welch, E., Damon, B., & Park, J. The quantitative effects of inclusion of fat on muscle diffusion tensor MRI measurements. *J Magn Reson Imaging.* **38** (5), 1292-1297 (2013).
46. Hernando, D. *et al.* Removal of olefinic fat chemical shift artifact in diffusion MRI. *Magn Reson Med.* **65** (3), 692-701 (2011).
47. Willcocks, R. J. *et al.* Longitudinal measurements of MRI-T_2 in boys with Duchenne muscular dystrophy: effects of age and disease progression. *Neuromuscul Disord.* **24** (5), 393-401 (2014).
48. Poon, C. S., & Henkelman, R. M. Practical T_2 quantitation for clinical applications. *J Magn Reson Imaging.* **2** (5), 541-553 (1992).
49. Does, M. D., & Gore, J. C. Complications of nonlinear echo time spacing for measurement of T_2. *NMR Biomed.* **13** (1), 1-7 (2000).
50. Poon, C. S., & Henkelman, R. M. 180° refocusing pulses which are insensitive to static and radiofrequency field inhomogeneity. *J Magn Reson.* **99** (1), 45-55 (1992).
51. Hollingsworth, K. G., de Sousa, P. L., Straub, V., & Carlier, P. G. Towards harmonization of protocols for MRI outcome measures in skeletal muscle studies: consensus recommendations from two TREAT-NMD NMR workshops, 2 May 2010, Stockholm, Sweden, 1-2 October 2009, Paris, France. *Neuromuscul Disord.* **22 Suppl 2**, S54-67 (2012).
52. Underhill, H. R., Rostomily, R. C., Mikheev, A. M., Yuan, C., & Yarnykh, V. L. Fast bound pool fraction imaging of the in vivo rat brain: Association with myelin content and validation in the C6 glioma model. *Neuroimage.* **54** (3), 2052-2065 (2011).
53. Smith, S. A. *et al.* Quantitative magnetization transfer characteristics of the human cervical spinal cord in vivo: application to adrenomyeloneuropathy. *Magn Reson Med.* **61** (1), 22-27 (2009).
54. Li, K. D. R., Dortch, R.D., Gochberg, D.F., Smith, S.A., Damon, B.M., Park, J.H. Quantitative magnetization transfer with fat component in human muscles. *Proc. 20th Ann Meeting ISMRM.* (2012).
55. Damon, B. M. Effects of image noise in muscle diffusion tensor (DT)-MRI assessed using numerical simulations. *Magn Reson Med.* **60** (4), 934-944 (2008).
56. Damon, B. M., Buck, A. K. W., & Ding, Z. Diffusion-tensor MRI-based skeletal muscle fiber tracking. *Imaging Med.* **3** (6), 675-687 (2011).
57. Froeling, M., Nederveen, A. J., Nicolay, K., & Strijkers, G. J. DTI of human skeletal muscle: the effects of diffusion encoding parameters, signal-to-noise ratio and T2 on tensor indices and fiber tracts. *NMR in Biomedicine.* **26** (11), 1339-1352 (2013).
58. Basser, P. J., & Pajevic, S. Statistical artifacts in diffusion tensor MRI (DT-MRI) caused by background noise. *Magn Reson Med.* **44** (1), 41-50 (2000).
59. Anderson, A. W. Theoretical analysis of the effects of noise on diffusion tensor imaging. *Magn Reson Med.* **46** (6), 1174-1188 (2001).
60. Saupe, N., White, L. M., Stainsby, J., Tomlinson, G., & Sussman, M. S. Diffusion tensor imaging and fiber tractography of skeletal muscle: optimization of B value for imaging at 1.5 T. *AJR Am J Roentgenol.* **192** (6), W282-290 (2009).
61. Levin, D. I., Gilles, B., Madler, B., & Pai, D. K. Extracting skeletal muscle fiber fields from noisy diffusion tensor data. *Med Image Anal.* **15** (3), 340-353 (2011).
62. Sinha, U., Sinha, S., Hodgson, J. A., & Edgerton, R. V. Human soleus muscle architecture at different ankle joint angles from magnetic resonance diffusion tensor imaging. *J Appl Physiol.* **110** (3), 807-819 (2011).
63. Jones, D. K., & Cercignani, M. Twenty-five pitfalls in the analysis of diffusion MRI data. *NMR Biomed.* **23** (7), 803-820 (2010).
64. Hamilton, G. *et al.* In vivo characterization of the liver fat ^{1}H MR spectrum. *NMR Biomed.* **24** (7), 784-790 (2011).
65. Hernando, D., Kellman, P., Haldar, J. P., & Liang, Z. P. Robust water/fat separation in the presence of large field inhomogeneities using a graph cut algorithm. *Magn Reson Med.* **63** (1), 79-90 (2010).
66. Hernando, D., Hines, C. D., Yu, H., & Reeder, S. B. Addressing phase errors in fat-water imaging using a mixed magnitude/complex fitting method. *Magn Reson Med.* **67** (3), 638-644 (2012).

Copyright © 2016 Journal of Visualized Experiments